Experimental and Numerical Investigation of Aerodynamic Performance for Airfoils with Morphed trailing-edges

Hasan Kamliya Jawahar[a,*], Qing Ai[a,**], Mahdi Azarpeyvand[a,]

[a] *University of Bristol, Bristol, United Kingdom, BS8 1TR*

Abstract

The aerodynamic performance of a NACA 0012 airfoil with morphing flaps were studied experimentally and numerically. Comprehensive aerodynamic measurements including pressure distribution, lift and drag forces and wake flow for airfoils with different morphing flap camber profiles were carried out over a wide range of angles of attack and chord-based Reynolds numbers. The results show that the morphing flap camber profiles significantly affect the aerodynamic performance and the downstream wake development. It was found that the highly cambered flap profiles provide higher lift coefficients compared to the moderately cambered flap profiles, with an insignificant reduction in the overall lift-to-drag ratio. Furthermore, the Q-criterion iso-surface results show that the separation near the trailing-edge is further delayed at high angles of attack for airfoils with high flap camber. This study shows that the effective design space of the morphing flaps can be expanded by taking into account the optimal aerodynamic performance requirements. The study also suggests that in order to achieve optimum aerodynamic performance, an independent surface morphing of the suction and pressure surface camber will be required to delay the onset of flow separation.

*PhD Student, Department of Aerospace Engineering

**Corresponding Author, PhD Student, Advanced Composites Centre for Science and Innovation (ACCIS)

Corresponding Author, Reader in Aeroacoustics, Department of Mechanical Engineering

Email addresses: hasan.kj@bristol.ac.uk (Hasan Kamliya Jawahar), Qing.ai@bristol.ac.uk (Qing Ai), m.azarpeyvand@bristol.ac.uk (Mahdi Azarpeyvand)

Keywords: Morphing, Airfoil, NACA 0012, Aerodynamics, CFD, DES,

Nomenclature

b	=	trailing-edge flap length, m
c	=	airfoil chord length, m
C_L	=	lift coefficient
$C_{L,max}$	=	maximum lift coefficient
C_D	=	drag coefficient
C_p	=	pressure coefficient
f	=	frequency, Hz
k	=	turbulent kinetic energy, m^2/s^2
l	=	airfoil span length, m
$L_x \times L_y \times L_z$	=	cell dimensions of computational grid
p_{ref}	=	reference pressure ($= 2 \times 10^{-5}$), Pa
Q	=	second invariant of the velocity-gradient tensor, $1/s^2$
Re_c	=	chord-based Reynolds number
S	=	wing area, m^2
U, U_∞	=	mean velocity, freestream velocity, m/s
$\overline{u'u'}$	=	streamwise Reynolds normal stress component
$\overline{v'v'}$	=	crosswise Reynolds normal stress component
x, y, z	=	streamwise, crosswise and spanwise coordinates, m
y^+	=	dimensionless wall distance
α	=	angle of attack, $^\circ$
β	=	morphing flap tip deflection angle, $^\circ$

1. Introduction

SUSTAINABLE and green energy including wind, solar and tidal energies have received significantly growing attention in past decades due to public concerns over air pollution. As the main source of renewable energy, wind energy industries have been facing disruptive technological revolutions including new materials, increased turbine size and novel control methods for improved efficiency and reduced cost [1]. In the past decade, the turbine size, both in terms of the tower height and turbine length, has been continuously increasing. As such, traditional control methods for wind turbine blades, the pitch and yaw, is losing their virtues considering the efficiency under control tasks like tower load control, gust load mitigation, turbine load management and fatigue load reduction. In order to address such issues, various new passive and active control methods have been considered. [2, 3, 4]

Featuring active and prompt responses to dynamic operation conditions, shape-adaptive structures are enabling wind turbine blades and aeroplane wings for improved performance with reduced weight and complexity penalty. Containing smooth geometric changes and continuous structural surfaces, these compliant light-weight control surfaces, which are increasingly known as morphing structures, remain conformal to the flow. As such, significant aerodynamic performance improvement and noise reduction are envisaged through morphing structures. The research motivation of this paper is to investigate the flow behaviours and performance enhancement mechanisms of morphing trailing-edges for airofoils, which is of fundamental importance in development and application of these novel high-lift devices for the next generation of wind turbine blades

Morphing structures have received significant interest from engineering community including wind energy, aviation and automobile industries, owing to their potential of high performance, low mechanism complexity and light-weight [5]. Current high-lift systems mainly consist of discrete rigid structured components, which are articulated around hinges and linkages to achieve wing shape change for flow control purposes. As such, the overall system complexity and structure

weight are considerably increased. Unlike the conventional high lift wing control surfaces, morphing structures usually use the conformal structural deformation to adaptively change wing shape, leading to simplified systems and reduced weight. Furthermore, the continuous deformation shape and smooth surface in morphing structures significantly reduce the associated aerodynamic noise, particularly the cavity type noise present in the hinged-flap configurations.

Studies have shown that the deformation shape and curvature of the morphing structure significantly affects the aerodynamic performance of the airfoils. Daynes *et al.*[4] showed that a morphing flap can provide the same change in the lift coefficient with a 30% less tip deflection compared to a hinged flap of equal flap length. This enhanced control effectiveness is believed to originate from the differing mean camber profiles between the airfoils. Wolff *et al.* [6] conducted a two-dimensional numerical investigation of a wind turbine airfoil fitted with morphing trailing-edges and found that the deformed morphing trailing-edge significantly affects the lift coefficient and stall behaviour of the airfoil. Results showed that the changes to the lift coefficient are dependent on the size, curvature and deflection angle of the deformed trailing-edge and strongly curved deformed trailing-edge can produce lower maximum lift-to-drag ratio and also increased the root bending moment coefficient compared to a gently curved deformed trailing-edge. Yokozeki *et al.*[7] developed a morphing airfoil concept using corrugated structures and wind tunnel tests of the demonstrator showed that the morphing wing presented superior properties in lift coefficient compared to a reference wing using the conventional flap, which was believed to result from the seamless morphing deformation. Ai *et al.*[8] proposed a novel morphing trailing-edge design using honeycomb core of axial variable stiffness and proved that introducing variable stiffness materials into the morphing structures could change the actuation energy of the system. Preliminary modelling has also shown that tailoring of the flap morphing profiles, significantly affects the aerodynamic and aeroacoustic performance of the airfoil. While the aerodynamic and aeroacoustic performance of other passive methods, such as serrations [9, 10, 11], surface conditioning [12] and porous treatments[13] etc,

have been the subject of much research, which the morphing trailing-edges have not received.

Even though continuous progress has been made on the structural aspects (*e.g.*, compliant mechanisms, smart actuators drivers, piezoelectric actuators *etc.*) of morphing devices over the last decade, detailed understanding and documentation of the aerodynamic performances of morphing structures are lacking. In this paper, detailed experimental and numerical studies have been performed to investigate the aerodynamic performance of morphing flaps on airfoils. A NACA 0012 airfoil is chosen for the tests and fitted with a series of flaps having different flap camber profiles but with the same flap-tip deflection and surface area. Wind tunnel tests including aerodynamic forces measurements and wake development analysis were carried out. High-quality CFD studies were also carried out to further investigate the flow structures, boundary layers and shear stresses influencing the aerodynamic performance.

2. Experimental and Computational Setup

2.1. Airfoil Model Setup

A NACA 0012 airfoil model with a chord length of $c = 0.2$ m and a span length of $l = 0.45$ m was manufactured using RAKU-TOOL® WB-1222 polyurethane board. The airfoil was designed with an interchangeable trailing-edge section with a chord-wise length of $b = 0.06$ m ($0.3c$), see Fig. 1. Several trailing-edge flap profiles with different flap angles were manufactured and tested. The flap deflection angle (β) is defined as the ratio of the morphing flap length, b and tip deflection length, while maintaining the same flap surface area, as shown in Fig. 1. The results from the preliminary aerodynamic and aeroacoustic study by Ai *et al.* [8] using novel morphing flaps were then used to design the morphing flap camber profiles used in the current experimental and computational study (see Fig. 1). The airfoils were tested with morphing flaps having different camber profiles for the deflection angles of, $\beta = 5°$ and $10°$. A close-up view of the flap is presented in Fig. 1, where the Hinged-Flap

airfoil represents a flap with typical hinged flap movement and the following Morphed-Flap (1-4) airfoil cases employ conformal morphing flap profiles with varying camber.

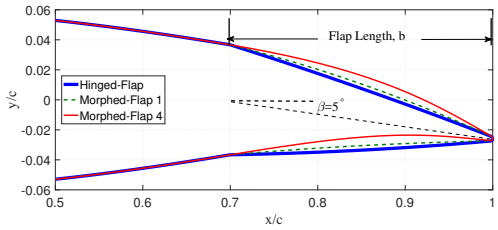

(a) $\beta = 5°$

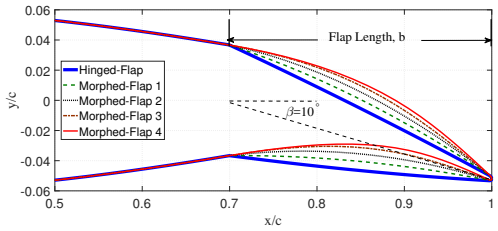

(b) $\beta = 10°$

Figure 1: Geometric details of NACA 0012 airfoil with different flap profiles employed in the current study for deflection angle $\beta = 5°$ (top) and $\beta = 10°$ (bottom).

2.2. Wind Tunnel and Experimental Setup

Aerodynamic force and wake flow measurements for the NACA 0012 airfoil fitted with different morphing flap camber profiles were carried out at the University of Bristol wind tunnel facility.

2.2.1. Force measurement setup

The aerodynamic force measurements were carried out in the large low-speed closed-circuit wind tunnel with an octagonal test section of 2.1 m × 1.5 m × 2 m, a contraction ratio of 3:1 and a stable working velocity range of 10 m/s to 60 m/s. Two circular side-plates with a radius of 0.17 m were used to reduce the three-dimensionality effects of the flow around the airfoil,

as shown in Fig. 2. The aerodynamic force measurements of the lift and drag forces were measured using an AMTI OR6-7-2000 force platform from Advanced Mechanical Technology Inc., mounted at the base of the set-up. The data were collected for a period of 30 s with a sampling frequency of 37 Hz obtained from a thorough uncertainty analysis of the collected data.

2.2.2. Pressure measurement setup

The pressure measurements were carried out in the low turbulence closed-circuit wind tunnel with an octagonal test section of 0.8 m × 0.6 m × 1 m, contraction ratio of 12:1, maximum velocity of 100 m/s and with turbulence level as low as 0.03% [14]. MicroDAQ pressure scanners were used for the measurements. The scanners have a full-scale accuracy of 0.05%. The pressure measurements were made at 40 pressure ports distributed over the surface of the airfoil and the exchangeable flaps, within $x/c = 0$ to 0.90. To obtain accurate pressure distribution results, measurements were carried out for a period of 60 s with a sampling frequency of 500 Hz. The averaged results were used to calculate the C_p pressure coefficient, presented in Sec.3.2.

2.2.3. Wake measurement setup

The wake flow behaviour was studied using hot-wire measurements, carried out at six different streamwise locations in the wake of the NACA 0012 airfoil with different trailing-edges. Measurements were performed in the open jet wind tunnel with a diameter of 1.1 m, with a maximum reliable speed of 30 m/s and a turbulence level of 0.05% at 20 m/s. The Dantec 55P16 single hot-wire probes were used to measure the steady flow velocity in the wake. The hot-wire probes were calibrated using a Dantec 54H10 two-point mode hot-wire calibrator. The data were collected for a time period of 20 s with a sampling frequency of 40 kHz.

2.3. Computational Setup

In addition to the experimental studies, Detached Eddy Simulations (DES) were also carried out to further investigate the flow characteristics around the hinged and morphed flaps. To initiate the simulations, Reynolds-averaged

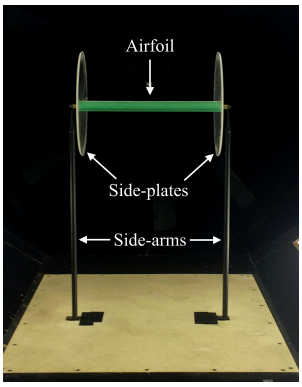

Figure 2: NACA 0012 airfoil with side-plates set up in the large low-speed closed-circuit wind tunnel.

Navier-Stokes (RANS) numerical simulations were performed using the OpenFOAM open source code and Spallart-Allmaras ($S-A$) turbulence model. The validated RANS [15, 16] results were then used as input for the DES simulations using the $S-A$ turbulence model. A three-dimensional multi-block structured C-H type mesh was used in the simulations, generated using the commercial software ICEM-CFD. After a domain independence study, the domain size was set to be $10c$ in the streamwise and $5c$ in the crosswise direction. The domain had a spanwise thickness of $0.1c$, which was deemed sufficient based on some similar studies [17, 18, 19, 20]. The cell distribution along the airfoil was $L_x \times L_y \times L_z = 260 \times 120 \times 32$. In order to accurately capture the near-the-wall boundary layer structures, the airfoil wall was set to have a $y^+ \approx 0.5 - 1$ with 40 grid points within $y = 0.035c$ close to the wall. The grid spacing along the streamwise direction corresponds to $x^+ \approx 30$ and is clustered toward the airfoil leading-edge and trailing-edge. To capture the wake behaviour accurately, an area of $1.5c$ downstream of the trailing-edge was densely populated with 200 grid points in the streamwise direction. In the spanwise direction, the grid spacing was uniformly distributed corresponding to $z^+ \approx 35$. A close-up view of the airfoil trailing-edge mesh is shown in Fig. 3. All the simulations were carried out for 30 flow through times (FTT) and the data were collected for only the last

10 FTT. A CFL value of $C_{max} \leq 1$ was maintained throughout the simulations with a time-step of $\Delta t = 2.75 \times 10^{-6}$ s.

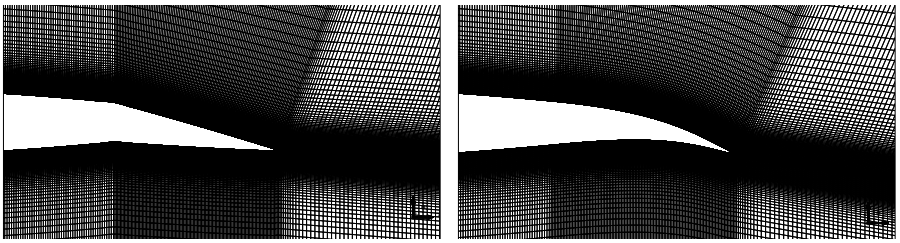

(a) Hinged-Flap (b) Morphed-Flap 4

Figure 3: NACA 0012 fitted with different morphing flap with a deflection angle of $\beta = 10°$ for the Hinged Flap and Morphed Flap 4 airfoil.

3. Results and Discussion

3.1. Force Measurements

The results of the lift and drag coefficients for the NACA 0012 airfoil fitted with various flap profiles (Hinged-Flap and Morphed-Flaps 1-4, see Fig. 1) with a flap deflection angle of $\beta = 5°$ and $10°$ at a freestream velocity of $U_\infty = 25$ m/s, corresponding to the chord-based Reynolds number of $Re_c = 3.5 \times 10^5$ are presented in Figs. 4 and 5, respectively. The airfoil was tested for angles of attack ranging from $\alpha = -5°$ to $20°$. The aerodynamic force measurements were carried out for three different freestream velocities ($U_\infty = 25$, 32 and 40 m/s) but results are only presented for $U_\infty = 25$ m/s as the lift and drag coefficients were found to be independent of the Reynolds number over this flow velocity range.

The lift and drag coefficient results presented in Figs. 4 and 5, clearly show that the variation in flap camber significantly alters the aerodynamic characteristics of the airfoil for the tested angles of attack. The C_L and C_D for the MF-4 airfoil (Morphed-Flap 4) with a flap deflection angle of $\beta = 5°$ (see Fig. 4), shows an increase in $C_{L,max}$ of up to 4% relative to the HF airfoil (Hinged-Flap). The

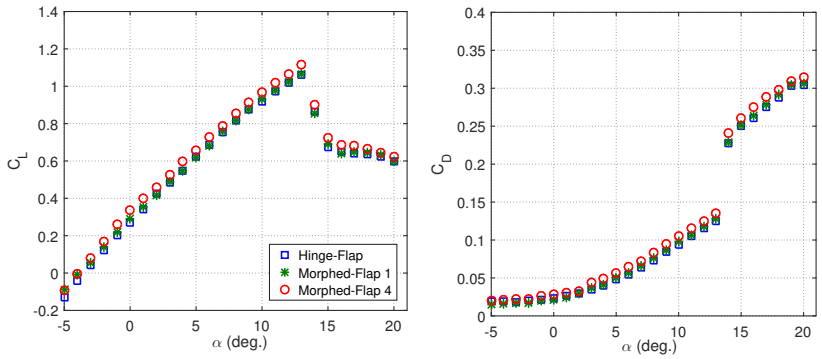

Figure 4: Lift and drag coefficient results for NACA 0012 airfoil fitted with various morphing flaps of $\beta = 5°$, at a freestream velocity of $U_\infty = 25$ m/s ($Re_c = 3.5 \times 10^5$).

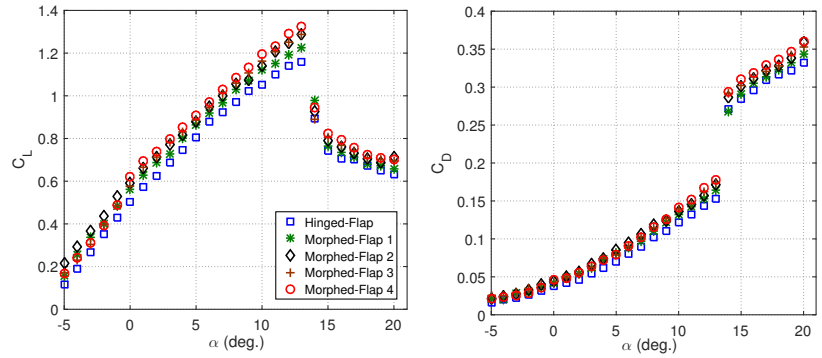

Figure 5: Lift and drag coefficient results for NACA 0012 airfoil fitted with various morphing flaps of $\beta = 10°$, at a freestream velocity of $U_\infty = 25$ m/s ($Re_c = 3.5 \times 10^5$).

MF-1 airfoil, which has a smaller flap camber relative to MF-4 airfoil, exhibits no change in C_L and C_D compared to the HF airfoil. The lift and drag coefficient results for $\beta = 10°$ presented in Fig. 5 show 13% increase in $C_{L,max}$ for the highly cambered MF-4 airfoil compared to the simple hinged flap HF airfoil at $\alpha = 13°$, just before stall. The C_L for HF airfoil has the lowest $\alpha - C_L$ curve out of all the tested camber profiles. The highest C_L was observed for the highly cambered MF-4 airfoil for the angles of attack ranging from $\alpha = 0°$ to 20°. However, at negative angles of attack, $\alpha = -5°$ to 0°, the MF-4 airfoil appears to have reduced C_L close to that of the MF-2 airfoil. Also, at negative

angles of attacks, from $\alpha = -5°$ to $0°$, the highest C_L was achieved by the MF-3 airfoil. Figure 5 also shows that at the stall angle of attack ($\alpha = 13°$), the C_D for the MF-4 airfoil increases by up to 14% relative to that of the HF airfoil. The overall drag of the morphing flap cases also increases with the increase in the flap camber profile. As can be seen, the MF-4 airfoil with the largest morphing flap camber results in the highest C_D compared to the other cases. The results show that the effect of flap camber on C_L and C_D at low deflection angle $\beta = 5°$ is not as significant as that of the higher deflection angle $\beta = 10°$. Results suggest that the effect of morphing profile will be even more important for larger deflection angles (β), which requires further investigation.

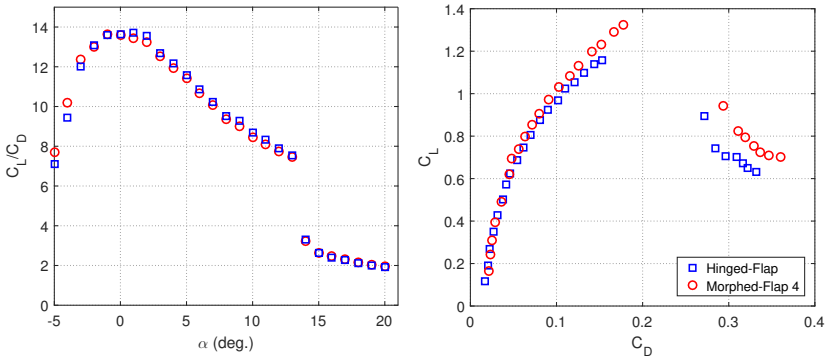

Figure 6: The lift-to-drag ratio for the Hinged Flap and Morphed Flap 4 airfoils with a deflection angle $\beta = 10°$, at a freestream velocity of $U_\infty = 25$ m/s ($Re_c = 3.5 \times 10^5$).

Figure 6 shows the lift-to-drag coefficient ratio (C_L/C_D) results for the HF and MF-4 airfoils. Results clearly show that there is no significant difference between the HF and MF-4 airfoil in terms of C_L/C_D. At negative angles of attack, $\alpha = -4°$, it can be seen that the MF-4 airfoil produces by about 8% greater C_L/C_D than that of the HF airfoil. However, this difference in C_L/C_D between the two cases decreases as the angle of attack is increased. The C_L/C_D difference between the airfoils decreases to insignificant values for all the positive angles of attack. The polar curves of C_L and C_D shown in Fig. 6 summarises the lift and drag performance of the HF and MF-4 airfoils, showing that the MF-4 airfoil has increased C_L and C_D as the angles of attack increases, especially close

to the stall angle. Results have also shown that the flap shape and deflection angle does not greatly change the stall angle, which is consistent with the results in the literature [21].

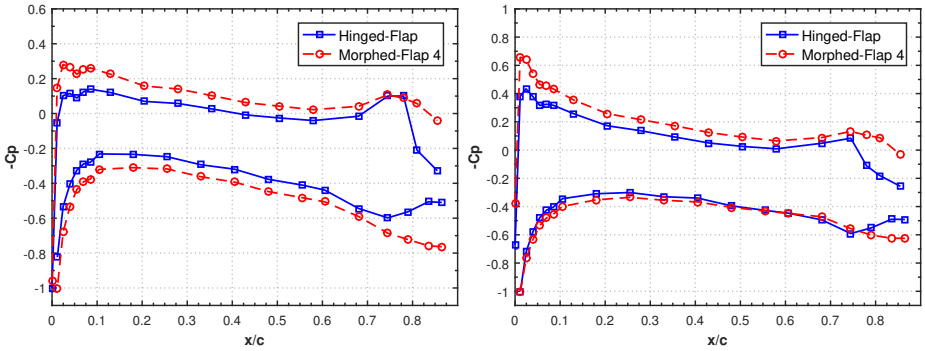

(a) $\alpha = 0°$ (b) $\alpha = 2°$

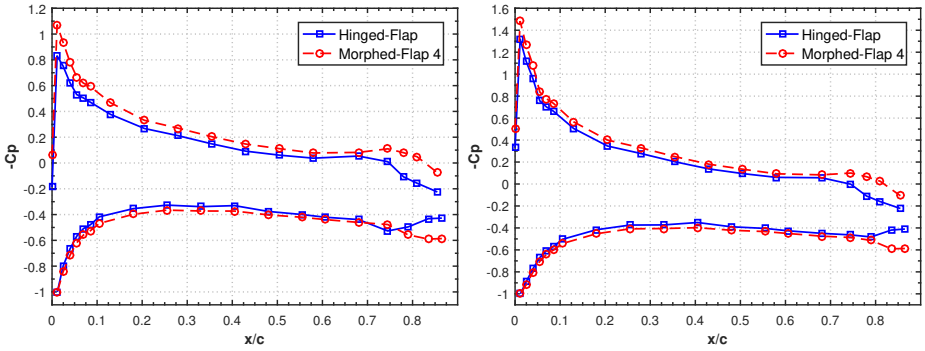

(c) $\alpha = 4°$ (d) $\alpha = 6°$

Figure 7: Pressure coefficient distribution over the Hinged Flap and Morphed Flap 4 airfoils at angles of attack $\alpha = 0°$, $2°$, $4°$ and $6°$, for a freestream velocity of $U_\infty = 20$ m/s ($Re_c = 2.6 \times 10^5$).

3.2. Pressure Distribution

The pressure distribution for both the HF and MF-4 airfoils are presented in Fig. 7 for the angles of attack, $\alpha = 0°$, $2°$, $4°$ and $6°$ at a freestream velocity of $U_\infty = 20$ m/s ($Re_c = 2.6 \times 10^5$). The overall trend of the pressure distribution results show a prominent difference between the HF and MF-4 airfoil at low

and moderate angles of attack. The difference between the two configurations, however, subsides as the angle of attack is increased. At low angles of attack, $\alpha = 0^\circ$ and 2°, the difference in the C_p suction peak close to the leading-edge for the HF airfoil is up to 40% lower than that of the MF-4 airfoil. This difference reduces to about 25% and 14% as the angle of attack is increased to $\alpha = 4^\circ$ and 6°, respectively and further reduces to about just 7% at $\alpha = 10^\circ$ (not presented for brevity). Prominent differences in C_p between the two configurations can also be observed around the flap region for all the angles of attack with larger differences seen on the suction-side. These differences in C_p distributions around the flap region are highly dependant on the angle of attack, as shown in Fig. 7. The presented results show that even a slight change of the flap camber shape with the same deflection angle can substantially change the pressure distribution and the suction peak at the leading-edge of the airfoil, especially at low angles of attack.

3.3. Wake Flow Development

The wake flow-field of both the HF and MF-4 airfoils was studied experimentally using hot-wire anemometry. Measurements were carried out at six locations within the airfoil wake region at the airfoil mid-span plane, namely $x/c = 1.01$, 1.065, 1.115, 1.125, 1.515 and 2.015, with the airfoil leading-edge assumed as the datum point for the coordinate system, as shown in Fig. 8. The tests were performed for four angles of attack, $\alpha = 0^\circ$, 2°, 4° and 6° at a freestream velocity of $U_\infty = 20$ m/s, corresponding to $Re_c = 2.6 \times 10^5$.

The wake velocity profiles for all the measurement planes and angles of attack are presented in Fig. 9. The wake velocity profiles for $\alpha = 0^\circ$ and 2° at the near-wake location $x/c = 1.01$ show a thicker boundary layer for the MF-4 airfoil compared to the HF airfoil. It can also be observed that the velocity gradient at $x/c = 1.01$ has increased at all angles of attack for the MF-4 airfoil compared to the HF airfoil. The results for all the presented angles of attack show that at further downstream locations the wake velocity for the MF-4 airfoil has an increased deflection angle compared to the HF airfoil and the level of deflection

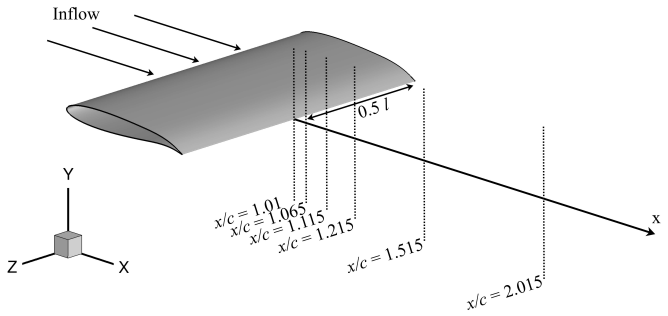

Figure 8: Airfoil coordinate system along with wake velocity measurements locations.

increases with increasing the angle of attack, especially at the far-wake locations $x/c = 1.125$, 1.515 and 2.015. The velocity deficit for MF-4 airfoil has slightly increased relative to the HF airfoil at all the downstream wake locations.

The non-dimensional turbulent kinetic energy (TKE) results calculated from the hotwire tests for the HF and MF-4 airfoils at the angles of attack $\alpha = 0°$, 2°, 4° and 6° are presented in Fig. 10. For the angles of attack $\alpha = 0°$ and 2°, at the location, $x/c = 1.01$ close to the trailing-edge, it can be observed that the TKE magnitude for the MF-4 airfoil is about 50% higher than that of the HF airfoil toward the suction side of the wake profile. For $\alpha = 0°$ and at further downstream location ($x/c = 1.065$), the TKE magnitude difference between the HF and MF-4 airfoils increases to 60%. The differences in the TKE magnitude between the two airfoils reduces at further far-wake downstream locations, $x/c = 1.215$, 1.515 and 2.015. It can also be observed that the MF-4 airfoil has a larger magnitude of TKE in the wake toward the pressure side compared to that of the HF airfoil. From the TKE magnitude peak location at the far-wake locations, $x/c = 1.215$, 1.515 and 2.015, previously mentioned increased wake flow deflection for the MF-4 airfoil can be observed readily. The results at higher angles of attack ($\alpha = 2°$, 4° and 6°) demonstrate that the TKE magnitude has a characteristic double peak behaviour, which was absent at the angle of attack $\alpha = 0°$. This is due to the interaction between the boundary layers developed over the airfoil pressure and suction side. The large difference

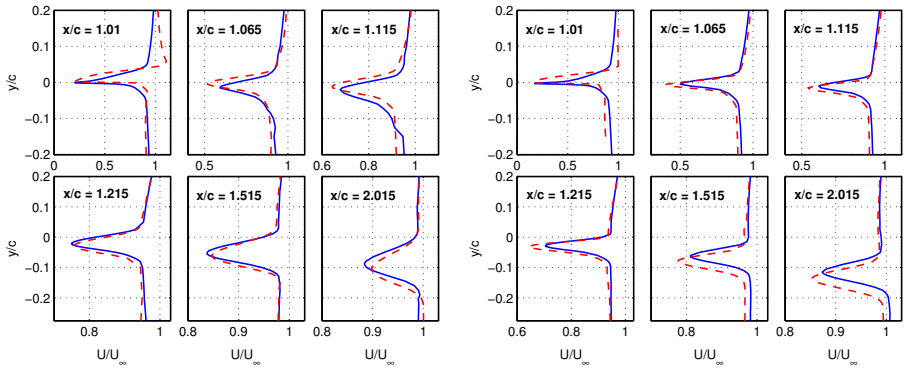

(a) $\alpha = 0°$ (b) $\alpha = 2°$

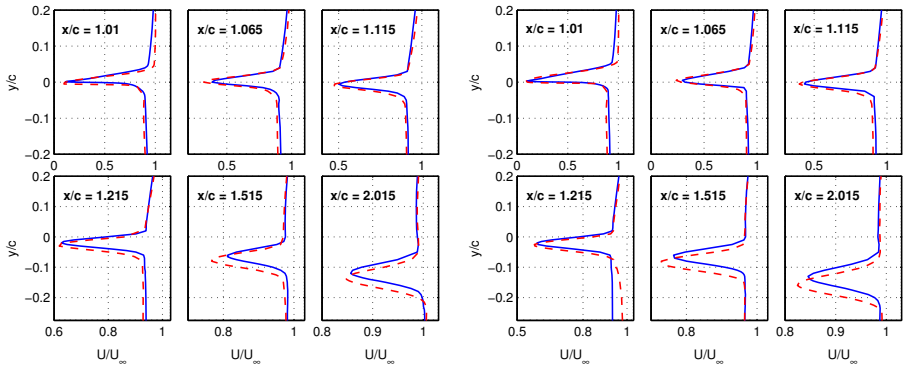

(c) $\alpha = 4°$ (d) $\alpha = 6°$

Figure 9: Wake velocity profiles at a freestream velocity of $U_\infty = 20$ m/s, for the Hinged-Flap — and Morphed-Flap 4 - - - airfoils.

in the TKE magnitude between the HF and MF-4 airfoils at $\alpha = 0°$ is no longer observed at higher angles of attack. However, there are still noticeable differences in TKE magnitude between the cases, with the MF-4 airfoil having larger TKE magnitude at far-wake locations. The increased deflection of the wake for the MF-4 airfoil compared to the HF airfoil can also be readily observed for low and moderate angles of attack at the far-wake the locations, $x/c = 1.215$, 1.515 and 2.015.

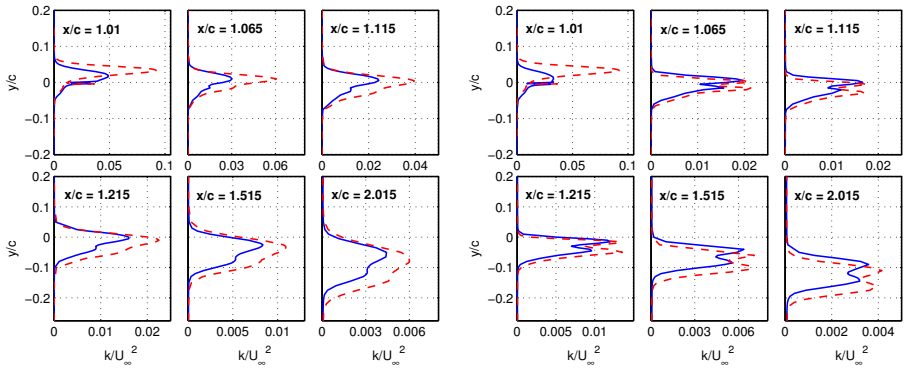

(a) $\alpha = 0°$ (b) $\alpha = 2°$

(c) $\alpha = 4°$ (d) $\alpha = 6°$

Figure 10: Wake turbulent kinetic energy profiles at a freestream velocity of $U_\infty = 20$ m/s, for the Hinged-Flap — and Morphed-Flap 4 - - - airfoils.

3.3.1. Wake Flow Structure

Besides the experimental results presented in the previous section, to gain a better understanding of the flow structures and the effect of morphing flaps, a detailed numerical investigation using the DES method was carried out for the two morphing flap configurations (HF and MF-4). The simulations were validated with the experimental measurements in the wake region. The validated computational results were used to further characterize the flow structure around the airfoil's morphing flap. For the purpose of brevity the results presented and discussed here are only for the angles of attack, $\alpha = 0°$ and $4°$ at

the freestream velocity of $U_\infty = 20$ m/s ($Re_c = 2.6 \times 10^5$).

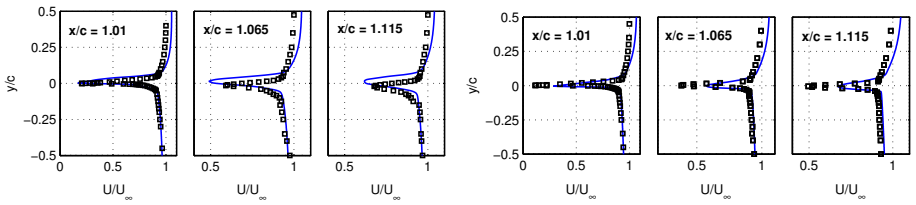

(a) Hinged-Flap, $\alpha = 0°$; DES —, Exp □

(b) Hinged-Flap, $\alpha = 4°$; DES —, Exp □

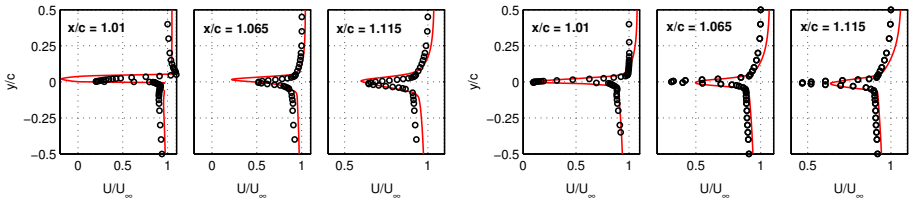

(c) Morphed-Flap 4, $\alpha = 0°$; DES —, Exp ○

(d) Morphed-Flap 4, $\alpha = 4°$; DES —, Exp ○

Figure 11: Comparison of wake velocity profiles obtained from DES simulation with experimental measurements for a freestream velocity of $U_\infty = 20$ m/s($Re_c = 2.6 \times 10^5$).

Results of the mean velocity profiles within the wake region for the HF and MF-4 airfoils for angles of attack $\alpha = 0°$ and $4°$ are presented in Fig. 11 along with the experimental measurements. It can be observed that the DES S-A model accurately predicts the velocity deficit and dip location at $\alpha = 0°$ compared against the experimental data at the near-wake locations, namely $x/c = 1.01$, 1.065 and 1.115, for the HF airfoil but slightly overpredicts the velocity deficit for the MF-4 airfoil. The mean velocity profiles for both the HF and MF-4 airfoils at $\alpha = 4°$ also show good agreement with the experimental data at $x/c = 1.01$ but slightly underpredicts the velocity deficit for the further downstream locations $x/c = 1.065$, 1.115 and $x/c = 2.015$. The experimentally measured dip location for both the HF and MF-4 airfoils have a larger flow deflection angle (flow turning angle) compared to the S-A model predictions. The discrepancies observed at far-wake locations are believed to be due to the open-jet wind tunnels effects and that such effects are not taken into account in the current simulations.

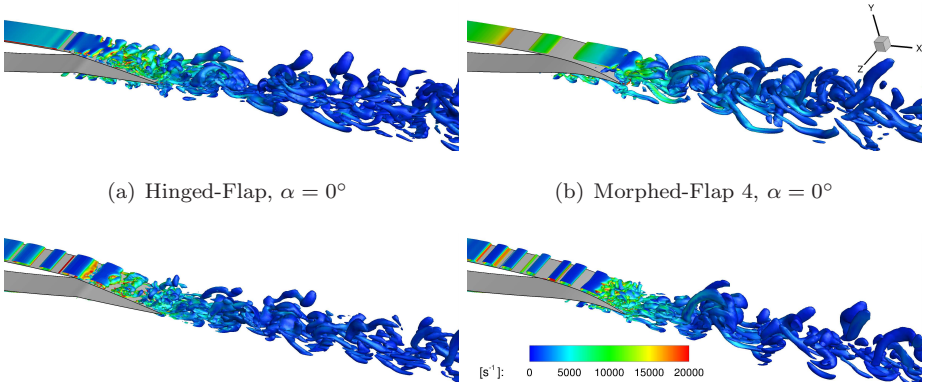

(a) Hinged-Flap, $\alpha = 0°$ (b) Morphed-Flap 4, $\alpha = 0°$

(c) Hinged-Flap, $\alpha = 4°$ (d) Morphed-Flap 4, $\alpha = 4°$

Figure 12: Iso-surfaces of Q-criterion of $Q = 1 \times 10^5 s^{-2}$ for Hinged Flap and Morphed Flap 4 airfoil with contours of vorticity magnitude for a freestream velocity of $U_\infty = 20$ m/s($Re_c = 2.6 \times 10^5$).

The iso-surfaces of the Q-criterion ($Q = 1 \times 10^5 s^{-2}$) with contours of the vorticity magnitude for the HF and MF-4 airfoils at the angles of attack $\alpha = 0°$ and $4°$ are shown in Fig. 12. At the angle of attack $\alpha = 0°$, the separation on the suction side occurs after the flap hinge ($x/c \approx 0.7$) for the HF airfoil, while no separation can be observed for the MF-4 airfoil, which can be attributed to the smooth cambered profile of the suction side of the morphed flap. For the HF airfoil, the separation on the pressure side occurs just before the hinge of the flap ($x/c \approx 0.65$) and reattaches to the surface right after the hinge ($x/c \approx 0.8$) before mixing into the airfoil wake. For the MF-4 airfoil, the separation on the pressure side occurs relatively early ($x/c \approx 0.8$) and reattaches only at the tip ($x/c \approx 0.95$) of the trailing-edge just before separating and mixing into the airfoil wake. This separation on the pressure side of the MF-4 airfoil with unsteady fluctuations between $x/c \approx 0.8$ and $x/c \approx 0.95$ could be the primary reason for the larger wake velocity deficit compared to HF airfoil, as mentioned previously in Sec.3.2. This also results in a wider wake region, with increased TKE (Sec.3.3) as discussed earlier.

From the iso-surface plots at $\alpha = 4°$ in Fig. 12 it can be observed that

for the HF airfoil case, the separation on the suction side occurs after the flap hinge point ($x/c \approx 0.8$). However, for the MF-4 airfoil shown in Fig. 12(d), the separation on the suction side is delayed and occurs closer to the trailing-edge ($x/c \approx 0.85$). In the case of $\alpha = 4°$, the recirculation on the pressure side of the HF airfoil is absent, while for the MF-4 airfoil the separation occurs at the same location as that of the suction side ($x/c \approx 0.85$) close to the trailing-edge before mixing into the airfoil wake. The onset of the separation on the pressure side of the MF-4 airfoil appears to be further delayed with the increase in the angle of attack. The separation region of the MF-4 airfoil on the pressure side always appears to be larger than that of the HF airfoil, resulting in an increased wake velocity deficit and TKE that adds to the increased form drag for the MF-4 airfoil, as observed earlier in Sec.3.1. The flow separation on the pressure side of the highly cambered flap profiles can be avoided by using independent surface morphing, since the cambered flap results in favourable delayed separation on the suction side but gives rise to an unfavourable recirculation on the pressure side. An optimum design requires a different camber profile for the pressure side to delay the onset of early separation and recirculation on the pressure side of the morphing flap. The iso-surface plots presented in Fig.12 also suggest that in the case of the HF and MF-4 airfoils at $\alpha = 4°$, the boundary layer develops Tollmien-Schlichting (TS) instability waves that occur as rolled-up two-dimensional vortical structures, after an initial stable state. These two-dimensional structures develop into turbulent three-dimensional eddies before reaching the trailing-edge. The two-dimensional vortical structures are also found on the pressure side of the MF-4 airfoil flap for both the presented angles of attack.

3.3.2. Boundary Layer Results

The non-dimensional boundary layer velocity profiles from the DES for the HF and MF-4 airfoils, at angles of attack $\alpha = 0°$ and $4°$ are presented in Figs. 13 and 14, respectively. The mean velocity profiles over the airfoil suction side, for $\alpha = 0°$, in Figs. 13(a) and 13(b), show prominent differences between

the HF and MF-4 airfoils. For the HF airfoil, the boundary layer separates immediately after the hinge at $x/c = 0.75$, after which the velocity changes direction at $x/c = 0.85$ and 0.90, indicating the emergence of a recirculation region. The flow then reattaches at $x/c = 0.95$, which can be determined by the sudden decrease in the velocity gradient ($\delta U/\delta y$). The negative velocities at the locations $x/c = 0.85$ and 0.90 can be attributed to the emergence of the vortices that leads to energy loss in the flow, as seen earlier in Fig. 10(a). These results correspond to flow separation previously seen in the flow visualisation of iso-contours in Fig. 12 and also seen in the C_p measurements in Fig. 7(a), where an increase in the suction peak over the flap region was observed. The boundary layer velocity results for the MF-4 airfoil in Fig. 13(b) show a steady growth in the boundary layer profile from the location $x/c = 0.65$ to 0.95 with no separation, as previously visualised in the iso-contours of Q-criterion in Fig. 12 and also seen in the C_p measurements in Fig. 7(a). This is due to the smoother flap curvature that aids in the increased velocity and lower pressure on the suction side of the flap. The velocity profiles on the suction side of the HF airfoil in Fig. 13(c) show a well-developed boundary layer with negative velocities at $x/c = 0.65$ and 0.75, indicating a small recirculation area at the flap hinge, a region where a decrease in surface pressure was previously observed in the C_p measurements in Fig. 7(a). A well-reattached flow can then be seen at downstream locations $x/c > 0.85$. The flow on the pressure side of the MF-4 airfoil in Fig. 13(d) shows a thicker boundary layer relative to the HF airfoil at $x/c = 0.65$ and 0.75 with negative velocities at $x/c = 0.75$. The flow appears to be completely separated at $x/c = 0.85$ but reattached at $x/c = 0.90$ and 0.95. This observation concurs with the iso-contour Q-criterion (Fig. 12) results previously discussed in Sec.3.3.1, where a large area of unsteady separated flow was observed over the pressure side of the MF-4 airfoil flap.

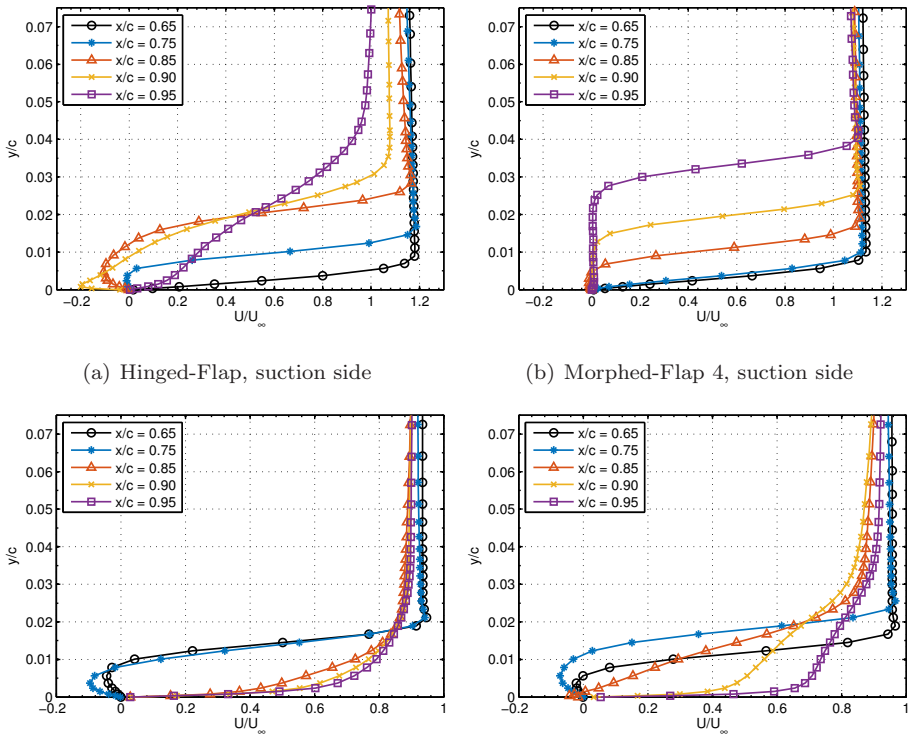

(a) Hinged-Flap, suction side

(b) Morphed-Flap 4, suction side

(c) Hinged-Flap, pressure side

(d) Morphed-Flap 4, pressure side

Figure 13: Boundary layer velocity profiles on the suction and pressure side at various streamwise locations of the Hinged Flap and Morphed Flap 4 airfoils at angle of attack $\alpha = 0^\circ$ for a freestream velocity of $U_\infty = 20$ m/s ($Re_c = 2.6 \times 10^5$).

The boundary layer results over the suction side of the HF and MF-4 airfoils at $\alpha = 4^\circ$ are presented in Figs. 14(a) and 14(b), respectively. For the HF airfoil, the flow over the suction side remains attached up to $x/c = 0.75$, after which the flow separates with decreasing velocity gradients at the following downstream locations. In the case of the MF-4 airfoil, the boundary layer thickness is smaller relative to the HF airfoil at the locations $x/c = 0.65$, 0.75 and 0.85 and the flow separation occurs at a further downstream location of $x/c = 0.90$. The velocity gradient at all locations for the MF-4 airfoil is higher than that of the HF airfoil. This suggests that the suction side of the MF-4 airfoil experiences a

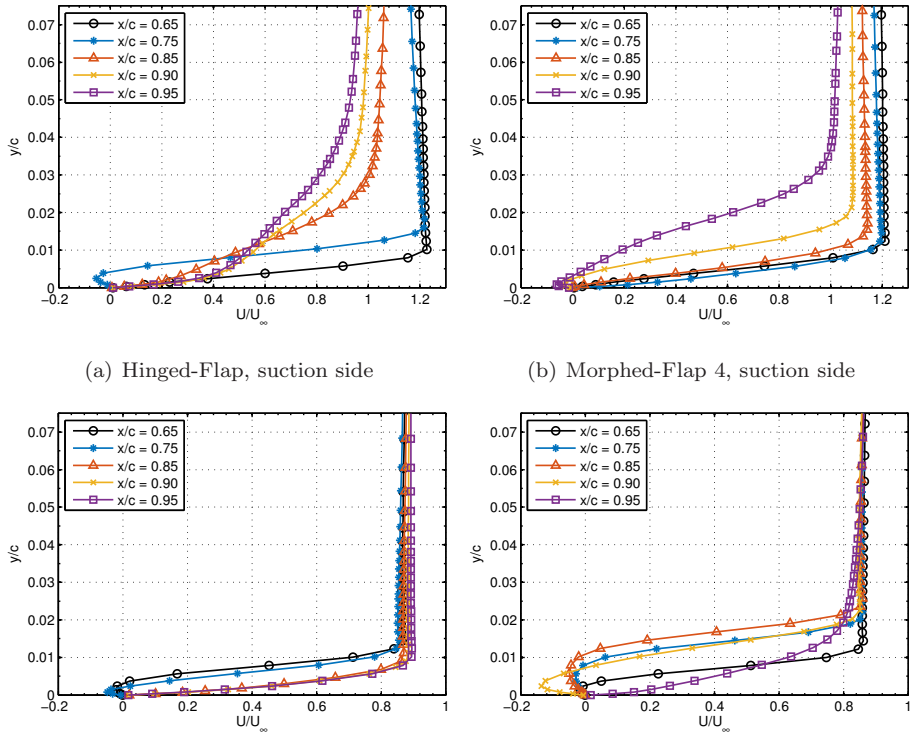

(a) Hinged-Flap, suction side

(b) Morphed-Flap 4, suction side

(c) Hinged-Flap, pressure side

(d) Morphed-Flap 4, pressure side

Figure 14: Boundary layer velocity profiles on the suction and pressure side at various streamwise locations of the Hinged Flap and Morphed Flap 4 airfoils at angle of attack $\alpha = 4°$, for a freestream velocity of $U_\infty = 20$ m/s ($Re_c = 2.6 \times 10^5$).

higher level of shear stress than the HF airfoil. The non-dimensional velocity above $y/c = 0.04$ at the locations, $x/c = 0.85$, 0.90 and 0.95 for the MF-4 airfoil is higher than that of the HF airfoil. This indicates higher velocity on the flap suction surface for the MF-4 airfoil than that of the HF airfoil, which also corresponds to the increased suction peak for the MF-4 airfoil seen earlier in the C_p measurements in Fig. 7(c). The non-dimensional boundary layer velocity profiles on the pressure side of both the HF and MF-4 airfoils are presented in Figs. 14(c) and 14(d). The results for the HF airfoil at $\alpha = 4°$ show a fully attached flow on the pressure side of the airfoil. However, the MF-4 airfoil at

$\alpha = 4°$, the results show a thicker boundary layer with negative velocities at almost all the locations from $x/c = 0.65$ to 0.90, which suggests a separated flow with a possible vorticity present on the pressure side of the MF-4 airfoil, as previously seen in the iso-contours (Fig. 12) and C_p measurements (Fig. 7(c)).

3.3.3. Reynolds Stress Tensor

The non-dimensional normal components of the Reynolds stress tensor ($\overline{u'u'}$,$\overline{v'v'}$) around the flap region for the HF and MF-4 airfoils are presented in Fig. 15. Results are presented for angles of attack $\alpha = 0°$ and 4° at a freestream velocity of $U_\infty = 20$ m/s. The same colour scale, except for Fig. 15(d), is used to facilitate comparison of the plots. For the HF airfoil, at $\alpha = 0°$, an area of increased velocity fluctuations ($\overline{u'u'}, \overline{v'v'}$) can be observed at $x/c = 0.85$, where reversed flow, indicating a recirculation region, was previously seen in the boundary layer results. The peak values of the normal stresses can be seen at about $x/c = 0.95$, where the separated boundary layer reattaches to the flap surface, as discussed previously in Sec.3.3.2. The velocity fluctuations over the flap suction side gradually increases from $x/c = 0.70$ until after the trailing-edge at $x/c = 1.15$. This indicates the flow separation over the HF airfoil flap suction side, which was also discussed earlier in the results of iso-contours, C_p and boundary layer measurements. For the MF-4 airfoil suction side, the areas of high energy are observed only at locations aft of the trailing-edge. Two distinct islands of $\overline{u'u'}$ can be seen close to the trailing-edge. These areas of high velocity fluctuations correspond to the high TKE seen in Fig. 10 and discussed in Sec.3.3. The increased stresses can also be observed on the pressure side of the MF-4 flap from $x/c = 0.8$ onwards, which can be attributed to the recirculation, as previously seen in the iso-contours and boundary layer results. The magnitude of the crosswise Reynolds stress ($\overline{v'v'}$) for the MF-4 airfoil in the wake at $\alpha = 0°$ is highest compared to all the cases. This is due to the large pressure difference at the trailing-edge caused by mixing of the attached high-velocity flow from the suction side with the low-velocity flow (due to recirculation) from the pressure side, which results in increased velocity fluctuations with wake shedding

aft of the trailing-edge point. From the results in Figs.15(a) and 15(b), it is evident that the high-velocity fluctuations on the suction side of the HF airfoil is absent for the MF-4 airfoil but a new unsteady region has appeared on the pressure side of the MF-4 airfoil, which was absent in the HF airfoil. This is due to the MF-4 airfoil flap pressure and suction surfaces following the same mean camber line. A slight modification on the pressure surface to have a lower mean camber, close to that of the HF or MF-1 airfoil (airfoil with a lower surface camber) would eliminate this localized unsteadiness in the velocity fields that arise due to the recirculation. The Reynolds stresses at $\alpha = 4^\circ$ for both the HF and MF-4 airfoils are localised on the suction side of the flap. The separation on the flap hinge at $x/c = 0.70$ for the HF airfoil and the delayed separation at $x/c = 0.90$ for MF-4 airfoil can be clearly seen here. This also agrees with the C_p results, where an increased pressure over flap surface was seen in Fig. 7(a). The results for the HF airfoil show elongated and increased velocity fluctuation regions extending from $x/c = 0.75$ until the trailing-edge, while the MF-4 airfoil produces a thicker high-intensity region starting from $x/c = 0.90$ and extending well into the wake region. The velocity fluctuations $(\overline{u'u'}, \overline{v'v'})$ at $\alpha = 4^\circ$ are much lower relative to $\alpha = 0^\circ$ on the pressure side of the airfoil for both the cases. This might be due to the pressure side of the airfoil being exposed to a larger volume of the incoming airflow.

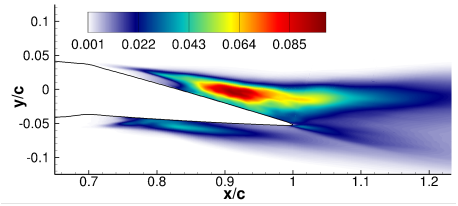

(a) $\overline{u'u'}/U_\infty^2$ - Hinged-Flap, $\alpha = 0°$

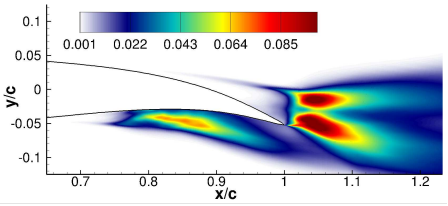

(b) $\overline{u'u'}/U_\infty^2$ - Morphed-Flap 4, $\alpha = 0°$

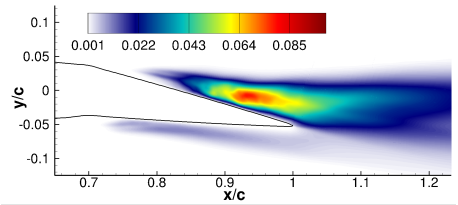

(c) $\overline{v'v'}/U_\infty^2$ - Hinged-Flap, $\alpha = 0°$

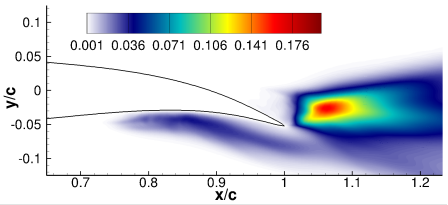

(d) $\overline{v'v'}/U_\infty^2$ - Morphed-Flap 4, $\alpha = 0°$

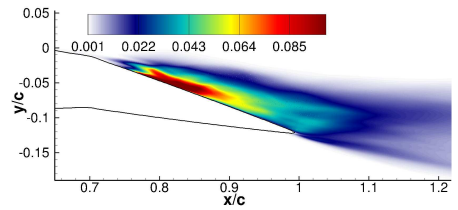

(e) $\overline{u'u'}/U_\infty^2$ - Hinged-Flap, $\alpha = 4°$

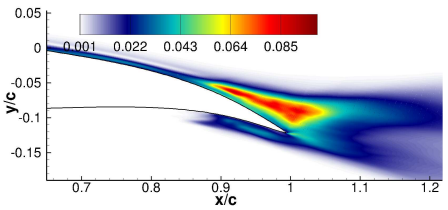

(f) $\overline{u'u'}/U_\infty^2$ - Morphed-Flap 4, $\alpha = 4°$

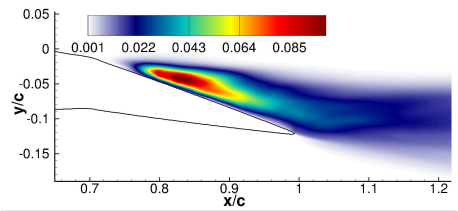

(g) $\overline{v'v'}/U_\infty^2$ - Hinged-Flap, $\alpha = 4°$

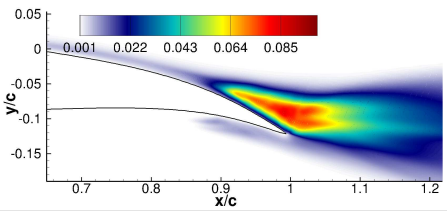

(h) $\overline{v'v'}/U_\infty^2$ - Morphed-Flap 4, $\alpha = 4°$

Figure 15: Streamwise and crosswise Reynolds stress distribution for the Hinged Flap and Morphed Flap 4 airfoils at angles of attack $\alpha = 0°$ and $4°$ for freestream velocity of $U_\infty = 20$ m/s ($Re_c = 2.6 \times 10^5$).

4. Conclusion

The aerodynamic performance of a NACA 0012 airfoil fitted with hinged- and morphed-flaps of various camber shapes were investigated using experimental and numerical techniques. The airfoil was tested for a freestream velocity of $U_\infty = 20$ m/s, corresponding to the chord-based $Re_c = 2.6 \times 10^5$. The aerodynamic force measurements have shown that the morphing flap with highly cambered profile (MF-4 airfoil) produces higher lift than that of simple hinged flap profile (HF airfoil). Even though higher C_L were observed for the MF-4 airfoil, the C_L/C_D results showed insignificant changes between the HF and MF-4 airfoil. The surface pressure measurements showed that the suction peak of the HF airfoil is up to 40% lower relative to the MF-4 airfoil at low angles of attack and that the difference between them decreases as the angle of attack is increased. The pressure distribution over the flap surfaces showed significant differences between the HF and MF-4 airfoil and they were highly dependant on angle of attack. Flow measurements using hot-wire anemometry were carried out to better understand the aerodynamic and flow characteristics of the hinged and morphed flaps. The results showed that the turbulent kinetic energy in the near-wake region closer to the suction side of the airfoil was higher for MF-4 airfoil compared to the HF airfoil. A detailed CFD simulation based on DES was carried out for $\alpha = 0°$ and $4°$ to visualise the flow structures and study the boundary layer and shear stresses for both of the cases. From these results, it was concluded that the increased drag at low angles of attack can be attributed to the recirculation and increased unsteady flow behaviour observed on the pressure side of the MF-4 airfoil that was absent in the HF airfoil. This study demonstrates that the changes in the camber profile of the flap with the same deflection angles can have a significant impact on the aerodynamic performance of airfoils. This study also shows that the simple change in the camber profile, i.e. independent movement of the top and bottom surfaces of the morphing flap, can have a significant impact on the aerodynamic performance of the airfoil and that an independent surface morphing structures, i.e. a higher

degree of freedom, may lead to a better aerodynamic performance of the airfoil.

References

[1] Kaldellis J.K, Zafirakis D. "The Wind Energy Revolution: A Short Review of a Long History", *Renewable Energy*, Vol. 36, pp: 1887-1901, 2011.

[2] Johnson S.J, Baker J.P, van Dam C.P, Berg D. "An Overview of Active Load Control Techniques for Wind Turbines with an Emphasis on Microtabs", *Wind Energy*, Vol. 13, pp: 239-253, 2009.

[3] Wolff T, Ernst B, Seume J.R. "Aerodynamic Behaviour of an Airfoil with Morphing trailing-edge for Wind Turbine Applications", *The Science of Making Torque from Wind 2014*, Copenhagen, Denmark, June 2014.

[4] Daynes, S., and Weaver, M.P., "A Morphing trailing-edge Device for a Wind Turbine", *Journal of Intelligent Material Systems and Structures*, Vol. 23, No. 6, pp: 691-701, 2012.

[5] Brand. C.B., and Seume, J.R. "Flaps for Wind Turbine Applications: Results of an Acoustic Study", *The European Wind Energy Association 2015 Annual Event*, Paris, France, Nov 2015.

[6] Wolff, T., Ernst, B., and Seume, J.R., "Aerodynamic Behaviour of an Airfoil with Morphing trailing-edge for Wind Turbine Application", *The Science of Making Torque from Wind 2014*, June 2014.

[7] Yokozeki, T., Sugiura,A., and Hirano,Y. "Development of Variable Camber Morphing Airfoil Using Corrugated Structure", *Journal of Aircraft*, Vol. 51, No. 3, pp:1023-1029, 2014.

[8] Ai, Q., Azarpeyvand, M., Lachenal, X., and Weaver, P., "Aerodynamic and Aeroacoustic Performance of Airfoils Using Morphing Structures", *Wind Energy*, Vol. 19, No. 7, pp: 1325-1339, 2016.

[9] Liu, X., Kamliya Jawahar, H., Azarpeyvand, M., and Theunissen, R., "Aerodynamic Performance and Wake Development of Airfoils with Serrated trailing-edges", *AIAA Journal*, Vol. 55, No. 11, November 2017.

[10] Lyu, B., Azarpeyvand, M., and Sinayoko, S., "On the noise prediction for serrated leading-edges", *Journal of Fluid Mechanics*, Vol. 826, pp: 205-234, 2017.

[11] Lyu, B., and Azarpeyvand, M., "Prediction of Noise from Serrated trailing-edges", *Journal of Fluid Mechanics*, Vol. 793, pp:556-588, 2016.

[12] Afshari, A., Azarpeyvand, M., Dehghan, A. A., and Szoke, M., "trailing-edge Noise Reduction Using Novel Surface Treatments", AIAA 2016-2834, 2016.

[13] Showkat Ali, S. A., Szoke, M., Azarpeyvand, M., and Ilario, C., "Trailing-edge Bluntness Flow and Noise Control Using Porous Treatments", AIAA 2016-2832, 2016.

[14] Barrett R.V., "Design and Performance of a New Low Turbulence Wind Tunnel at Bristol University", *The Aeronautical Journal*, Vol. 88, No. 873, pp. 86-90, March 1984.

[15] Ai, Q., Kamliya Jawahar, H., and Azarpeyvand, M., "Experimental Investigation of Aerodynamic Performance of Airfoils Fitted with Morphing Trailing-edges", AIAA 2016-1563, 2016.

[16] Kamliya Jawahar, H., Ai, Q., and Azarpeyvand, M., "Experimental and Numerical Investigation of Aerodynamic Performance of Airfoils Fitted with Morphing Trailing-edges", AIAA 2017-3371, 2017.

[17] Mellen C. P., Frograve J., hlich., and Rodi W., "Lessons from LESFOIL Project on Large-Eddy Simulation of Flow Around an Airfoil", *AIAA Journal*, Vol. 41, No. 4, pp. 573-581, 2003.

[18] Wolf W. R., Azevedo J. L., and Lele S. K., "Convective Effects and the Role of Quadrupole Sources for Aerofoil Aeroacoustics", *Journal of Fluid Mechanics*, vol. 708, pp. 502-538, 2012.

[19] Winkler J., Moreau S., and Carolus T., "Airfoil trailing-edge Blowing: Broadband Noise Prediction from Large-Eddy Simulation", *AIAA Journal*, Vol. 50, No. 2, pp. 294-303, 2012.

[20] Kamliya Jawahar H., Lin Y., and Savill M., "Large Eddy Simulation of Airfoil Self-noise using OpenFOAM", *Aircraft Engineering and Aerospace Technology*, Vol. 90, Issue. 1, 2018.

[21] Carl J. Wenzinger, "Wind-Tunnel Investigation of Ordinary and Split Flaps on Airfoils of Different Profile, *NACA-Report-No.544*, 1937.